PAPER

Check for updates

Free-standing N,Co-codoped TiO₂ nanoparticles for LiO₂-based Li–O₂ batteries†

Wen-Long Bai, [a] Shu-Mao Xu, [a] Cheng-Yang Xu, [b] Qiang Zhang, [a] Hong-Hui Wang, [a] Zhen Zhang, [a] Xin Chen, [a] Sheng-Yang Dong, [b] Yu-Si Liu, [a] Zhi-Xin Xu, [a] Xiao-Gang Zhang, [b] Zhen Wang, [c] Kai-Xue Wang [*a] and Jie-Sheng Chen [a]

Li–O₂ batteries based on lithium superoxide (LiO₂) would address the issues of significant polarization, low energy density and inferior cycle performance. However, LiO₂ as an intermediate product in the discharge process is very active and could be readily disproportionated into Li₂O₂. Thus, it is challenging to find an appropriate cathode catalyst, which can stabilize the active discharge product LiO₂. In this work, heteroatom N and Co codoped titanium dioxide nanoparticles grown on carbon fibers (N,Co-TiO₂/CFs) are fabricated and employed as a non-noble metal cathode catalyst for Li–O₂ batteries. LiO₂ formed in the Li–O₂ batteries can be repeatedly charged and discharged with a very low charge potential of approximately 3.0 V (*vs.* Li/Li⁺). N,Co-codoped TiO₂ is proposed to be responsible for the generation of stable LiO₂. This discovery opens a new way for the fabrication of non-noble metal cathode catalysts for high-performance LiO₂-based Li–O₂ batteries.

1. Introduction

Li–O₂ batteries with high theoretical energy density comparable to that of gasoline have drawn considerable attention in the past decade.[1–5] However, the poor conductivity and sluggish oxygen evolution reaction (OER) of the discharge product, Li₂O₂, are the major issues that impact the performance of Li–O₂ batteries.[6,7] The inherent poor conductivity and insolubility of Li₂O₂ in the electrolyte would lead to a high overpotential, consequently resulting in the decomposition of the electrolyte and the occurrence of side reactions. To address these issues, strategies, such as the morphological regulation of Li₂O₂ and exploitation of bifunctional catalysts and redox mediators, have been developed.[8–21] Although remarkable progress has been made recently,[22–26] it is still challenging to design a new path toward high-efficiency Li–O₂ batteries.

As revealed by theoretical calculation, LiO₂ has a short O–O bond distance (1.3–1.4 Å) and unpaired electron spin, leading to excellent conductivity, 10⁸ times greater than that of Li₂O₂.[21,27–36]

ᵃShanghai Electrochemical Energy Devices Research Center, School of Chemistry and Chemical Engineering, Shanghai Jiao Tong University, Shanghai 200240, P. R. China. E-mail: k.wang@sjtu.edu.cn

ᵇJiangsu Key Laboratory of Materials and Technology for Energy Conversion, College of Material Science and Engineering, Nanjing University of Aeronautics and Astronautics, Nanjing, 210016, P. R. China

ᶜKey Laboratory of Materials Processing and Mold of Ministry of Education, Zhengzhou University, Zhengzhou, 450001, P. R. China

† Electronic supplementary information (ESI) available. See DOI: 10.1039/c9ta08684f

During the discharge process, the generation of LiO₂ involves the transfer of only one electron per formula, different from the two-electron transfer process of Li₂O₂, making the formation of LiO₂ more kinetically preferred. The low activation energy for LiO₂ results in a low theoretical charging potential of 2.76 V (*vs.* Li/Li⁺), which is lower than that of Li₂O₂ (2.96 V). The reduced reaction potential in the electrochemical processes is beneficial to the stability of the electrolyte and the current collector. Therefore, it is proposed that the control of the discharge product to LiO₂, instead of Li₂O₂, might be an effective strategy to enhance the electrochemical properties of Li–O₂ batteries. However, as an intermediate of the discharge product, LiO₂ is thermodynamically unstable and the disproportionation of LiO₂ into Li₂O₂ usually occurs. Thus, it is full of difficulties to stabilize the discharge product LiO₂ during the discharge process. In addition, O₂⁻ generated in the discharge process is highly active in a protic solvent, accelerating the decomposition of the nucleophilic electrolyte.

It is reported that LiO₂ can only be stabilized at low temperatures or under O₂-rich conditions.[36] When forming clusters, LiO₂ in high electronic spin states and planar ring-shaped structures is thermodynamically more stable than the LiO₂ dimer.[27,35] Under such conditions, LiO₂ could be the primary discharge product because of the low O₂ desorption barrier and slow disproportionation to Li₂O₂. Recently, a graphene composite with surface supported Ir nanoparticles was prepared and proven to be favorable for the nucleation and growth of a crystalline LiO₂ phase in Li–O₂ batteries.[31] An Ir₃Li intermetallic compound with an orthorhombic lattice, similar

23046 | *J. Mater. Chem. A*, 2019, **7**, 23046–23054

This journal is © The Royal Society of Chemistry 2019

to that of LiO_2, was detected during the first discharge. The similar lattice might indicate that Ir nanoparticles are the active sites for the nucleation and growth of crystalline LiO_2. More recently, 3D porous Pd–rGO composites were prepared and employed as the cathode catalysts for reversible Li–O_2 batteries.[29] Amorphous LiO_2 detected during the discharge process is believed to contribute to the superb oxygen evolution reactivity and high electrical conductivity of the cathode. However, noble metals are usually involved in these cathodes for Li–O_2 batteries based on LiO_2. The development of non-noble-metal-based cathode catalysts to facilitate the formation and stabilization of the intermediate LiO_2 phase and simultaneously alleviate the side reactions of the electrolytes and LiO_2 is still highly desirable.

Herein, nanosheets composed of N,Co-codoped TiO_2 nanoparticles grown on carbon fibers (N,Co-TiO_2/CFs) have been designed and prepared hydrothermally. When used directly as a non-noble-metal-based cathode catalyst for Li–O_2 batteries, high electrochemical performance, including an ultra-low charge potential ($\sim$3.0 V) and excellent rate performance, was achieved. The formation and decomposition of the amorphous intermediate LiO_2 phase during the discharge process are demonstrated by Raman spectroscopy, galvanostatic intermittent titration (GITT) analysis, and differential electrochemical mass spectrometry (DEMS). The high electrochemical performance of the batteries is therefore ascribed to the LiO_2 phase. The adsorption energies between LiO_2 and electrodes were simulated by density functional theory (DFT) calculations based on first principles. The N,Co-TiO_2/CF cathode based on TiO_2 and carbon materials opens a new avenue for the development of high-performance non-noble-metal-based cathode catalysts for LiO_2-based Li–O_2 batteries.

2. Experimental

2.1 Preparation

Preparation of the TiO_2/CF cathode. The TiO_2/CF cathode was prepared by a seed-assisted method reported in the literature.[37,38] Carbon fibers were washed ultrasonically with acetone and then distilled water. After drying at 80 °C in a vacuum oven, the cleaned CFs were immersed in a 0.1 M tetrabutyl titanate solution and then dried in an air oven at 80 °C. The dried CFs were subsequently heated in a tube furnace at 450 °C for 1 h to generate the TiO_2/CF precursor. 0.66 mL of tetrabutyl titanate was dissolved in a solution containing 30 mL distilled water and 30 mL concentrated hydrochloric acid under stirring. Then, the tetrabutyl titanate solution with the TiO_2/CF precursor was transferred into a 100 mL Teflon-lined stainless steel autoclave and heated at 160 °C for 12 h. After cooling down naturally to room temperature, the product was washed several times with distilled water and dried at 80 °C for 24 h. Finally, the samples were calcined in air at 500 °C for 2 h.

Preparation of the N,Co-TiO_2/CF cathode. TiO_2/CFs, 0.2 g of $Co(NO_3)_2$, and NH_4F with a solution of 10 M NaOH were loaded into a Teflon-lined stainless steel autoclave and heated at 130 °C for 72 h.[39] The obtained samples were rinsed with 0.05 M HCl, ethanol, and distilled water successively, followed by drying at

70 °C overnight. Then, the hydrothermally treated TiO_2/CF precursor was loaded into a 50 mL Teflon-lined autoclave with a solution containing 25 mL of distilled water and 1.2 mL of HF and reacted at 180 °C for 24 h. N,Co-TiO_2/CF cathodes were obtained by rinsing the hydrothermal products with distilled water and ethanol several times and drying at 80 °C.

2.2 Characterization

X-ray diffraction (XRD) patterns were recorded on a D/max 2550VL/PC X-ray diffractometer (Rigaku, Japan) equipped with Cu Kα radiation ($\lambda = 1.5418$ Å, 40 kV, 30 mA). Raman spectra were obtained using an inVia-reflex micro-Raman spectrometer (Renishaw, UK) with a 532 nm wavelength incident laser. The discharge products were attached to a coverslip with a polyimide film in order to avoid contact with air. One side of the polyimide film can be used for XRD analyses and the other side for Raman analyses. The morphology and structure of the samples were observed on a field-emission scanning electron microscope (FESEM, NOVA Nano SEM 230, FEI, USA) and a JEM-2100F TEM (JEOL, Japan) operating at 200 kV. X-ray photoelectron spectroscopy (XPS) analyses were carried out on an AXIS Ultra DLD. Thermogravimetric analysis was conducted on a Q5000IR (TGA Instruments, USA) with a heating rate of 5 °C min^{-1} from 30 °C to 800 °C in air. UV-vis diffuse reflectance spectra were recorded on a UV-vis spectrophotometer (PERKI-NELMER, Lambda 750S). DEMS experiments were conducted in a custom-built electrochemical flow cell (similar to EL-Cell, ECC-DEMS), attached in-line with a gas flow controller (MT-52, Horiba Metron) and a quadrupole mass spectrometer (HPR-1100, Inficon). The gas flow is 2 mL min^{-1}. A mixture of Ar/O_2 (8 : 2, v/v) was used as the carrier gas during the discharge process, while high-purity Ar was used during the charge process. A constant current density of 0.2 mA cm^{-2} is utilized in the DEMS test and the capacity is set at 0.6 mA h.

2.3 Electrochemical measurements

N,Co-TiO_2/CFs and TiO_2/CFs were used directly as free-standing cathodes for Li–O_2 batteries without the involvement of any polymer binders and conducting agents. The electrochemical performances of the cathodes were evaluated using CR2025 coin cells (X2 Labwares) including a lithium metal anode (15 mm in diameter), an electrolyte infiltrated glass fiber separator, a 1.0 M bis(trifluoromethane) sulfonimide lithium/tetraethylene glycol dimethyl ether (LiTFSI/TEGDME) electrolyte, and the as-prepared cathodes. The loading mass of active materials on N,Co-TiO_2/CFs was determined to be 0.3 mg according to the thermogravimetric analyses conducted in air (ESI, Fig. S1†). The Li–O_2 batteries were assembled in an argon-filled glove box with water and oxygen contents less than 1 ppm. The cathode side exposed to oxygen had several machine-drilled holes. An O_2-filled glove box was utilized to guarantee a test environment and avoid the impact of H_2O or CO_2. The galvanostatic charge–discharge performance was studied in the potential range from 2.0 to 4.3 V using a battery tester LAND CT2001 at room temperature. CV was carried out within a voltage range of 2.0 to 4.5 V (0.1 mV s^{-1}). The cycling ability

was measured at a current density of 100 mA g^{-1}, with a cut-off capacity of 500 and 1000 mA h g^{-1}, respectively. The whole electrochemical calculation was on the basis of N and Co co-doped titanium dioxide nanoparticles on the CFs. Electrochemical impedance spectroscopy (EIS) measurements were conducted on a CHI 660E with a frequency extent of 0.01–10^5 Hz. Linear sweep voltammetry (LSV) was carried out using a CHI 660C.

2.4 DFT calculation

Density functional theory (DFT) calculations based on first principles were used to estimate the adsorption energies of LiO$_2$ on different catalysts, including TiO$_2$/CFs, N-TiO$_2$/CFs, Co-TiO$_2$/CFs, and N,Co-TiO$_2$/CFs. All spin-polarized calculations were conducted using the Vienna *Ab initio* Simulation Package (VASP). A kinetic energy cutoff of 500 eV was selected. Atomic relaxation calculation was performed by using the conjugate gradient method until a convergence criterion of 1 meV Å^{-1} and the total stress tensor was within 0.01 GPa of the target value.

3. Results and discussion

The typical procedure for the preparation of nanosheets composed of N,Co-codoped TiO$_2$ nanoparticles on carbon fibers is shown in Scheme 1. First, TiO$_2$ nanorod arrays were grown on the surface of carbon fibers (TiO$_2$/CFs) through a seed-assisted hydrothermal method.[37–39] The as-prepared TiO$_2$/CF sample was reacted with Co(NO$_3$)$_2$ and NH$_4$F in a NaOH aqueous solution under hydrothermal conditions at 150 °C for 72 h. Then, the obtained intermediate product was hydrothermally treated in the presence of HF at 180 °C for 24 h to prepare N,Co-codoped TiO$_2$ nanosheets on CFs (N,Co-TiO$_2$/CFs). N,Co-TiO$_2$/CFs was used directly as a binder-free air cathode for Li–O$_2$ batteries. For comparison, N-doped TiO$_2$/CF and Co-doped TiO$_2$/CF samples were also prepared through the same hydrothermal reaction

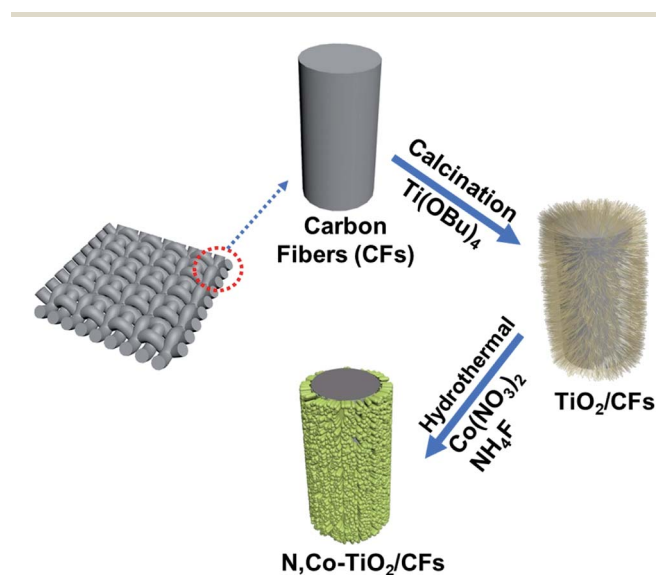without the involvement of cobalt nitrate and NH$_4$F, respectively.

In the XRD patterns of N,Co-TiO$_2$/CFs (Fig. 1a), diffraction peaks at 27.4°, 36.0°, 41.2°, 54.3°, 56.6°, and 69.0° (2θ) can be assigned to the (110), (101), (111), (211), (220), and (301) planes of rutile TiO$_2$ (JCPDS no. 75-1748). The peak at 25.7° is attributed to the carbon fibers with a low graphitization degree. The XRD analysis suggests that highly crystalline rutile TiO$_2$ was generated on the carbon fibers after the hydrothermal reaction.[40–45] In the Raman spectra of N,Co-TiO$_2$/CFs (Fig. 1b), the peaks at 447 and 612 cm^{-1} are assigned to E$_g$ and A$_{1g}$ vibration modes of rutile TiO$_2$. The broad peak at 236 cm^{-1} is attributable to the composite spectral peak of rutile TiO$_2$, one of the Raman spectrogram characteristic peaks of rutile TiO$_2$. The peaks that appear at 1597 and 1336 cm^{-1} are assigned to the G-band and D-band, respectively, of the carbon fibers. The relative intensity of the G-band and D-band is quite low, which might be due to the TiO$_2$ coating on the carbon fiber surface. A peak at 691 cm^{-1} is observed in the Raman spectrum of N,Co-TiO$_2$/CFs. This peak might be induced by the formation of Co–O bonds, suggesting the successful introduction of Co into TiO$_2$.[44]

The morphologies of TiO$_2$/CFs and N,Co-TiO$_2$/CFs were observed by scanning electron microscopy (SEM). For TiO$_2$/CFs, TiO$_2$ nanorods with an average diameter of 200 nm are vertically and homogenously grown onto the CFs (ESI, Fig. S2†). After the hydrothermal treatments, these nanorod arrays transform into nanoparticles uniformly coated on the carbon fibers (Fig. 1c and d). The carbon fibers with nanoparticles coated can provide a large void space for the loading of discharge products. The transmission electron microscopy (TEM) image of N,Co-TiO$_2$/CFs further reveals that the nanoparticles have an average particle size of 40 nm (Fig. 1e). Distinct lattice fringes with an interplanar spacing of 3.3 Å are observed in the high-resolution TEM (HRTEM) image (Fig. 1f), attributed to the (110) planes of rutile TiO$_2$. The elemental mapping of N,Co-TiO$_2$/CFs reveals the good distribution of N and Co over the samples (ESI, Fig. S3†), indicating the successful doping of TiO$_2$.

XPS spectra of N,Co-TiO$_2$/CFs are shown in Fig. S4.† In the high resolution Ti 2p spectrum (ESI, Fig. S4b†), the peaks at 459.9 and 465.5 eV can be ascribed to Ti 2p$_{3/2}$ and Ti 2p$_{1/2}$, respectively. The Co 2p peaks can be deconvoluted into two components at 786 and 798 eV, assignable to Co 2p$_{3/2}$ and Co 2p$_{1/2}$, respectively (ESI, Fig. S4c†). In the high resolution of N 1s spectrum (ESI, Fig. S4d†), the peak at 399.5 eV can be attributed to O–Ti–N bonds.[39] A binding energy of 401.5 eV is derived from surface adsorbed nitrogen species. The doping amount of N and Co is 0.4 at% and 0.1 at%, respectively.

To demonstrate the successful doping of N and Co into rutile TiO$_2$, we conducted UV-vis diffuse reflectance spectroscopy of TiO$_2$/CFs and N,Co-TiO$_2$/CFs (ESI, Fig. S5†). In the spectrum of N,Co-TiO$_2$/CFs (ESI, Fig. S5a†), a strong absorption is observed in the visible light range from 400 to 580 nm. However, no such absorption is detected in the same range for TiO$_2$/CFs. As a direct-gap semiconductor, the band gap of rutile TiO$_2$ was calculated by using approximate Kubelka–Munk eqn (1):

$$(\alpha h\nu/K)^2 = h\nu - E_g \qquad (1)$$

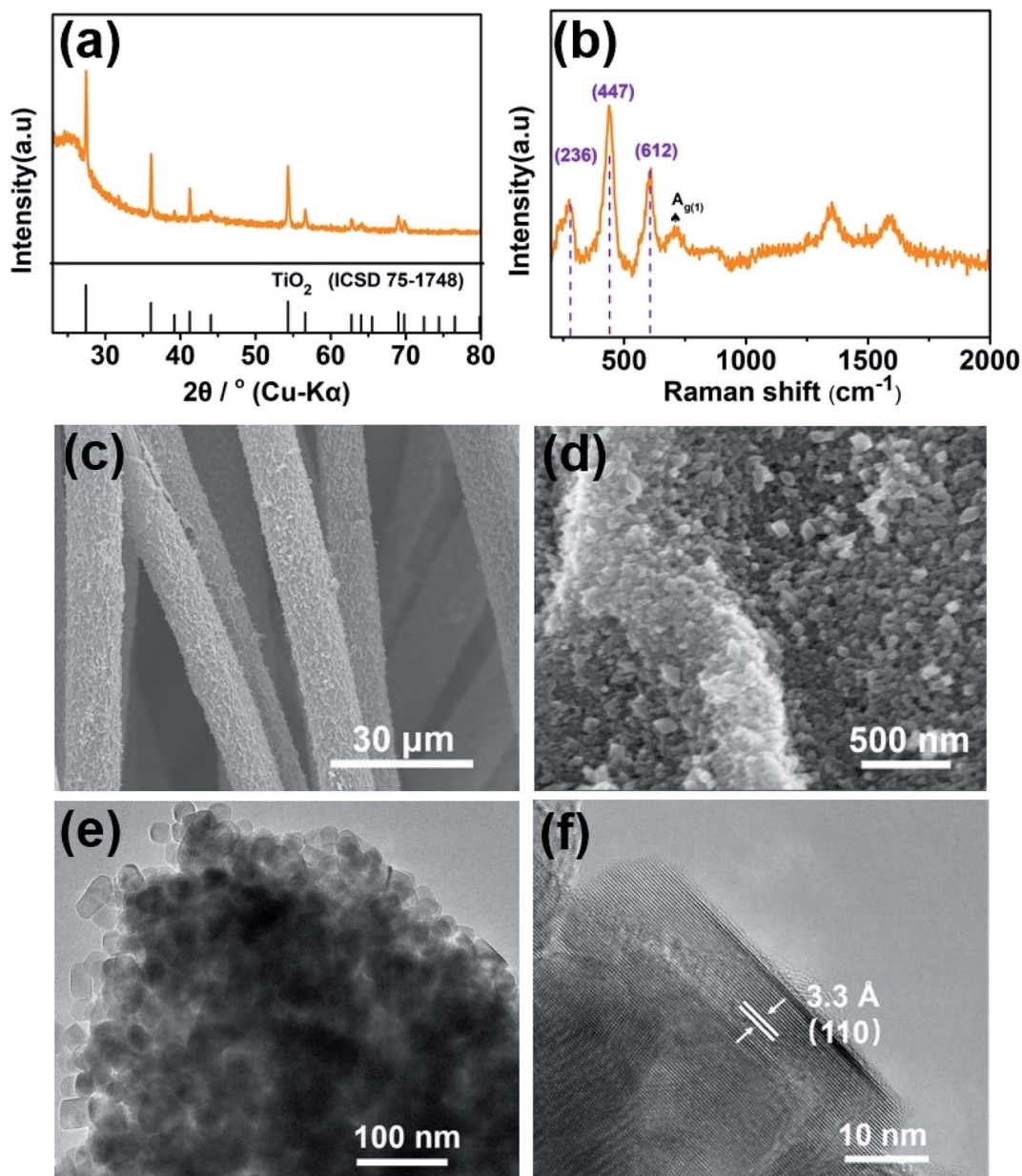**Scheme 1** Schematic illustration of the preparation of N,Co-TiO$_2$/CFs.

23048 | *J. Mater. Chem. A*, 2019, **7**, 23046–23054

This journal is © The Royal Society of Chemistry 2019

Fig. 1 Characterization of N,Co-TiO$_2$/CFs: (a) XRD pattern. (b) Raman spectrum. (c and d) SEM. (e) TEM, and (f) HRTEM images.

where α is optical absorption and K is a constant. The band gap of N,Co-TiO$_2$/CFs is approximately 2.0 eV, lower than that of TiO$_2$/CFs (2.9 eV) (ESI, Fig. S5b†). The decreased band gap of N,Co-TiO$_2$/CFs might be induced by the N and Co doping.

The electrochemical performance of free-standing N,Co-TiO$_2$/CF and TiO$_2$/CF cathodes was evaluated by cyclic voltammetry (CV) at a constant scan rate of 0.1 mV s^{-1} (Fig. 2a and ESI, Fig. S6†). The onset potential of the oxygen reduction reaction (ORR) of N,Co-TiO$_2$/CFs is around 2.76 V, which is identical to the reaction equilibrium potential of LiO$_2$. This result might indicate the formation of LiO$_2$ during the ORR. The onset potential of the oxygen evolution reaction (OER) is around 2.80 V, which is much lower than that of TiO$_2$/CFs (more than 4.0 V).[29] The reduced overpotential suggests that the ORR and OER

activities of N,Co-TiO$_2$/CFs are significantly improved. In the CV profile of N,Co-TiO$_2$/CFs, the cathodic peak at 2.26 V is attributed to oxygen reduction. The anodic peak at 3.5 V is ascribed to the decomposition of discharge products. The cathodic and anodic peak currents of N,Co-TiO$_2$/CFs are −1.75 and 1.80 mA, respectively, higher than those of TiO$_2$/CFs, suggesting an increased catalytic performance of N,Co-TiO$_2$/CFs.

Galvanostatic discharge/charge experiments of N,Co-TiO$_2$/CFs and TiO$_2$/CFs were carried out at a current density of 100 mA g^{-1} within 2.25 to 4.3 V (Fig. 2b). N,Co-TiO$_2$/CFs delivers a discharge capacity of 5400 mA h g^{-1} with a discharge voltage plateau of 2.75 V. During the subsequent charging process, N,Co-TiO$_2$/CFs shows a highly reversible specific capacity of 5300 mA h g^{-1}, giving a coulombic efficiency of 98%. The

This journal is © The Royal Society of Chemistry 2019

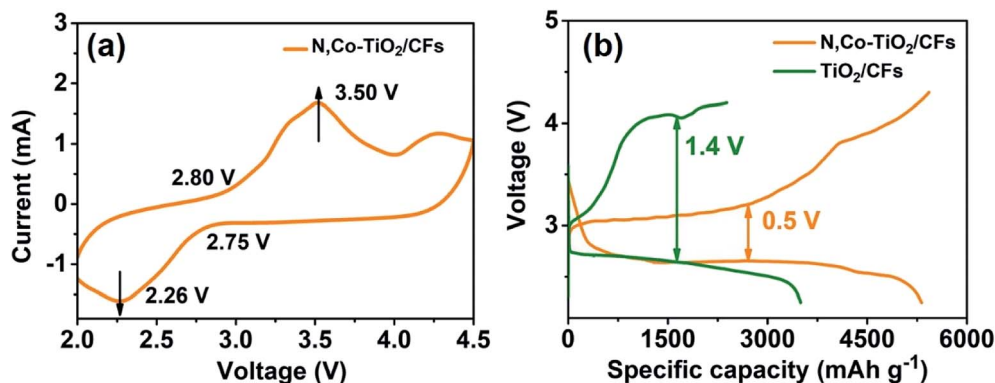J. Mater. Chem. A, 2019, 7, 23046–23054 | 23049

Fig. 2 (a) Cyclic voltammetry (CV) profile of the N,Co-TiO$_2$/CF cathode at a constant scan rate of 0.1 mV s^{-1}. (b) The full discharge/charge profiles of N,Co-TiO$_2$/CFs and TiO$_2$/CFs at a current density of 100 mA g^{-1}.

discharge/charge overpotential is only 0.5 V, much lower than that of Li–O$_2$ batteries based on Li$_2$O$_2$ (1.4 V). A distinct plateau located at approximately 3.0 V is in the charge profile of N,Co-TiO$_2$/CFs, giving a very low charge overpotential of 0.1 V. Such a low charge overpotential might suggest the formation of LiO$_2$, in good agreement with those reported in the literature.[29,31]

The corresponding XRD patterns of N,Co-TiO$_2$/CFs and TiO$_2$/CFs after the 1st discharge are shown in Fig. 3a. Diffraction peaks at 23°, 32.7°, and 47.1° (2θ) assignable to the (002), (201), and (004) planes, respectively, of hexagonal Li$_2$O$_2$ (JCPDS no. 73-1640) can be observed on the TiO$_2$/CF cathode, indicating the formation of crystalline Li$_2$O$_2$ during the discharge process. No distinct peaks are detected in the discharged N,Co-TiO$_2$/CFs, indicating that no crystalline Li$_2$O$_2$ or LiO$_2$ (the LiO$_2$ peaks are based on a theoretical XRD pattern (ESI, Fig. S7†) derived from DFT (density functional theory)-predicted crystalline LiO$_2$) forms during the discharge process. As reported by Liu and co-workers,[29] amorphous LiO$_2$ would be generated upon discharging. The absence of diffraction peaks might indicate that the discharge product, LiO$_2$, formed in this work is also amorphous. In the Raman spectrum of the discharged electrodes of N,Co-TiO$_2$/CFs (Fig. 3b), a band at 1123 cm^{-1}, characteristic of LiO$_2$, is observed. N,Co-TiO$_2$/CFs was used directly as free-standing cathodes for Li–O$_2$ batteries without the involvement of any polymer binders such as PVDF, so the band at 1123 cm^{-1} is assigned to LiO$_2$ rather than the decomposition of PVDF.[46] This result further confirms the generation of LiO$_2$ and is consistent with the results reported in the literature.[31,32] In the Raman spectra of the discharged TiO$_2$/CF cathode (Fig. 3b), a small peak at 830 cm^{-1} typical for the stretching frequencies of Li$_2$O$_2$ is detected, indicating the formation of Li$_2$O$_2$. Raman analyses indicate the formation of LiO$_2$ during the discharge process of the N,Co-TiO$_2$/CF cathode.

The existence of the discharge product LiO$_2$ on N,Co-TiO$_2$/CFs was also confirmed by an experiment in which O$_2$ is replaced by Ar after being discharged to 2500 mA h g^{-1} (Fig. 3c). After switching from O$_2$ to Ar when discharged to 2500 mA h g^{-1}, no obvious capacity decay is observed in the subsequent discharge. The capacity detected in the inert Ar atmosphere

might be derived from the transformation of LiO$_2$ into Li$_2$O$_2$ (eqn (2)):

$$Li^+ + e^- + LiO_2 \rightarrow Li_2O_2 \qquad (2)$$
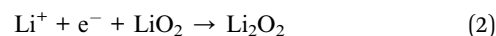
The stability of LiO$_2$ was investigated using a galvanostatic intermittent titration technique (GITT). In the discharge voltage profile of N,Co-TiO$_2$/CFs (Fig. 3d), the equilibrium voltage is approximately 2.76 V in the different states of the discharge process, consistent with the theoretical formation potential of LiO$_2$. The result shows that N,Co-TiO$_2$/CFs has a critical influence on stabilizing the discharge product LiO$_2$ and preventing its subsequent disproportionation reaction into Li$_2$O$_2$. Raman spectra of the N,Co-TiO$_2$/CF cathode were collected after being discharged for 5 h and 10 h, corresponding to 500 mA h g^{-1} and 1000 mA h g^{-1}, respectively (ESI, Fig. S8†). The band at 1123 cm^{-1} assigned to LiO$_2$ can be observed in the Raman spectra, confirming the generation of LiO$_2$.

Linear sweep voltammetry (LSV) further confirms the existence of LiO$_2$ by its phase transformation process under different discharge times from 2.8 V to 4.4 V. As shown in Fig. S9,† when discharged at 50 mV s^{-1} for 5 h and 15 h, peaks located at 3.35 V and 3.4 V are observed respectively, corresponding to the decomposition of LiO$_2$. After 30 h of deep discharge, an anodic peak appears at a higher potential (3.9 V), indicating the formation of Li$_2$O$_2$ on the cathode during the discharge process. The accumulation might be derived from the transformation of LiO$_2$ into Li$_2$O$_2$ (2LiO$_2$ → Li$_2$O$_2$ + O$_2$) during long-term discharge. The result is in good agreement with the phase transformation of LiO$_2$ in O$_2$ and Ar.

The morphology of discharge products on the surface of N,Co-TiO$_2$/CFs and TiO$_2$/CFs was observed by SEM. After the 1st discharge, sphere-like LiO$_2$ with a diameter of approximately 2.0 μm is observed uniformly coated on the surface of N,Co-TiO$_2$/CFs (Fig. 3e). The morphology of discharge products is different from the conventional toroidal morphology of the discharge product Li$_2$O$_2$. The spherical discharge product might indicate a novel growth mechanism in the presence of N,Co-TiO$_2$/CFs. Disc-like Li$_2$O$_2$ can be found on the surface of the TiO$_2$/CF nanofibers after the 1st discharging process (Fig. 3f). The size of

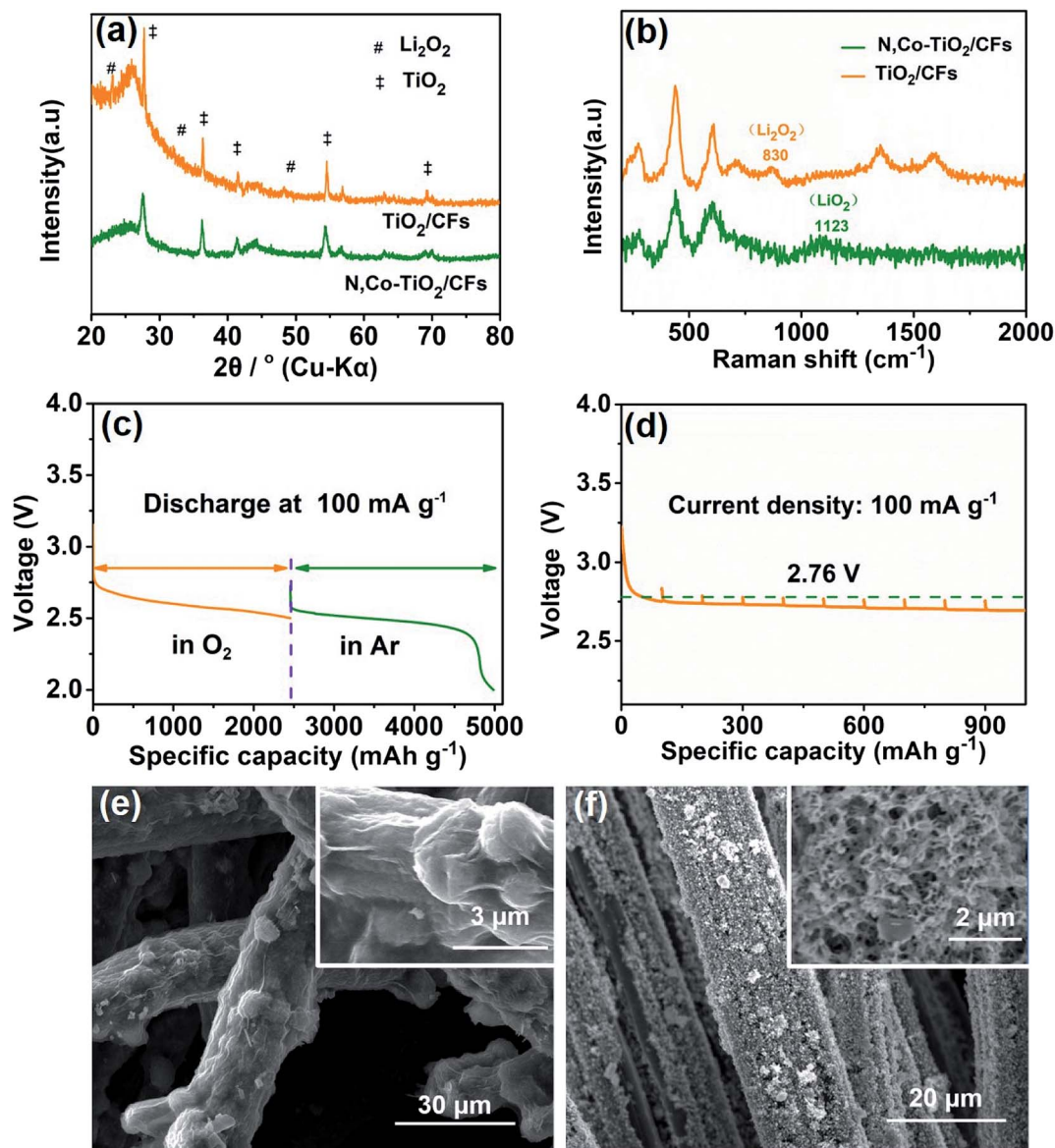**Fig. 3** (a) XRD patterns and (b) Raman spectra of the discharged TiO_2/CF and $N,Co-TiO_2/CF$ cathodes. (c) The voltage plots for $N,Co-TiO_2/CFs$ discharged first in O_2 to a capacity of 2500 mA h g^{-1} and then discharged in Ar. (d) The galvanostatic intermittent titration (GITT) profile of the $N,Co-TiO_2/CF$ cathode. SEM images of discharged (e) $N,Co-TiO_2/CFs$ and (f) TiO_2/CFs.

these discharge products is approximately 400 nm, much smaller than LiO_2. The enlarged size and unique morphology of LiO_2 might be attributable to Co and N co-doping into TiO_2. As revealed by the SEM observation, the spherical discharge products on the surface of $N,Co-TiO_2/CFs$ are decomposed after the 1st charge (ESI, Fig. S10a†). However, residual disc-like discharge products are still observed on the surface of TiO_2/CF cathodes (ESI, Fig. S10b†). This result demonstrated the excellent OER catalytic activity of the $N,Co-TiO_2/CF$ cathode.

The discharge products of $N,Co-TiO_2/CF$ and TiO_2/CF cathodes were further investigated by X-ray photoelectron spectroscopy (ESI, Fig. S11†). In the high resolution Li 1s spectrum of discharged TiO_2/CFs, a peak located at 55.5 eV is observed, corresponding to the Li–O bonds of Li_2O_2. However, the Li 1s
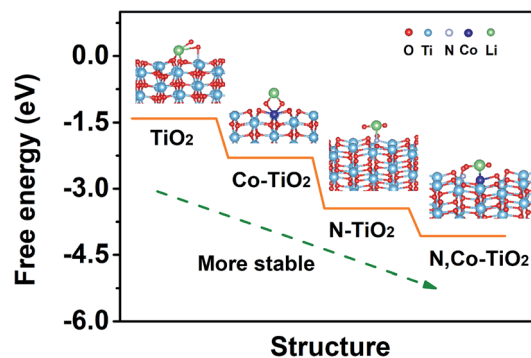

Fig. 4 Adsorption of LiO_2 on the (110) surface of TiO_2/CFs, $N-TiO_2/CFs$, $Co-TiO_2/CFs$ and $N,Co-TiO_2/CFs$.

This journal is © The Royal Society of Chemistry 2019

J. Mater. Chem. A, 2019, **7**, 23046–23054 | **23051**

binding energy of the Li–O bonds of discharged N,Co-TiO$_2$/CFs is blue shifted to approximately 63.2 eV. The 7.7 eV blue shift might be a result of the strong electron-withdrawing effect in superoxide ions. The Li 1s XPS spectra of discharged N,Co-TiO$_2$/CF and TiO$_2$/CF cathodes also indicate the formation of LiO$_2$ upon discharging in N,Co-TiO$_2$/CFs.

Differential quantitative mass spectrometry (DEMS) was employed to monitor the number of evolved and consumed O$_2$ molecules. The experiment was performed using high current densities and capacities (0.2 mA cm^{-2} and 0.6 mA h) to enable the measurement of variational O$_2$. During the discharge process, remarkable O$_2$ consumption was observed (ESI, Fig. S12a†). The

average O$_2$ consumption rate calculated is approximately 2.7 × 10^{-10} mol min^{-1}, giving an e$^-$/O$_2$ ratio of 1.11. In the subsequent charge process, the release of O$_2$ was detected (ESI, Fig. S13b†). The evolution rate of O$_2$ detected by DEMS is approximately 2.4 × 10^{-10} mol min^{-1} with an e$^-$/O$_2$ ratio of 1.04. According to the equation Li + O$_2$ ↔ LiO$_2$, the charge-to-mass ratio is 1 e$^-$/O$_2$. These charge-to-mass ratios of discharge and charge processes are consistent with the charge-to-mass ratio of the formation of LiO$_2$, further indicating the formation of LiO$_2$ during the discharge process of N,Co-TiO$_2$/CFs.

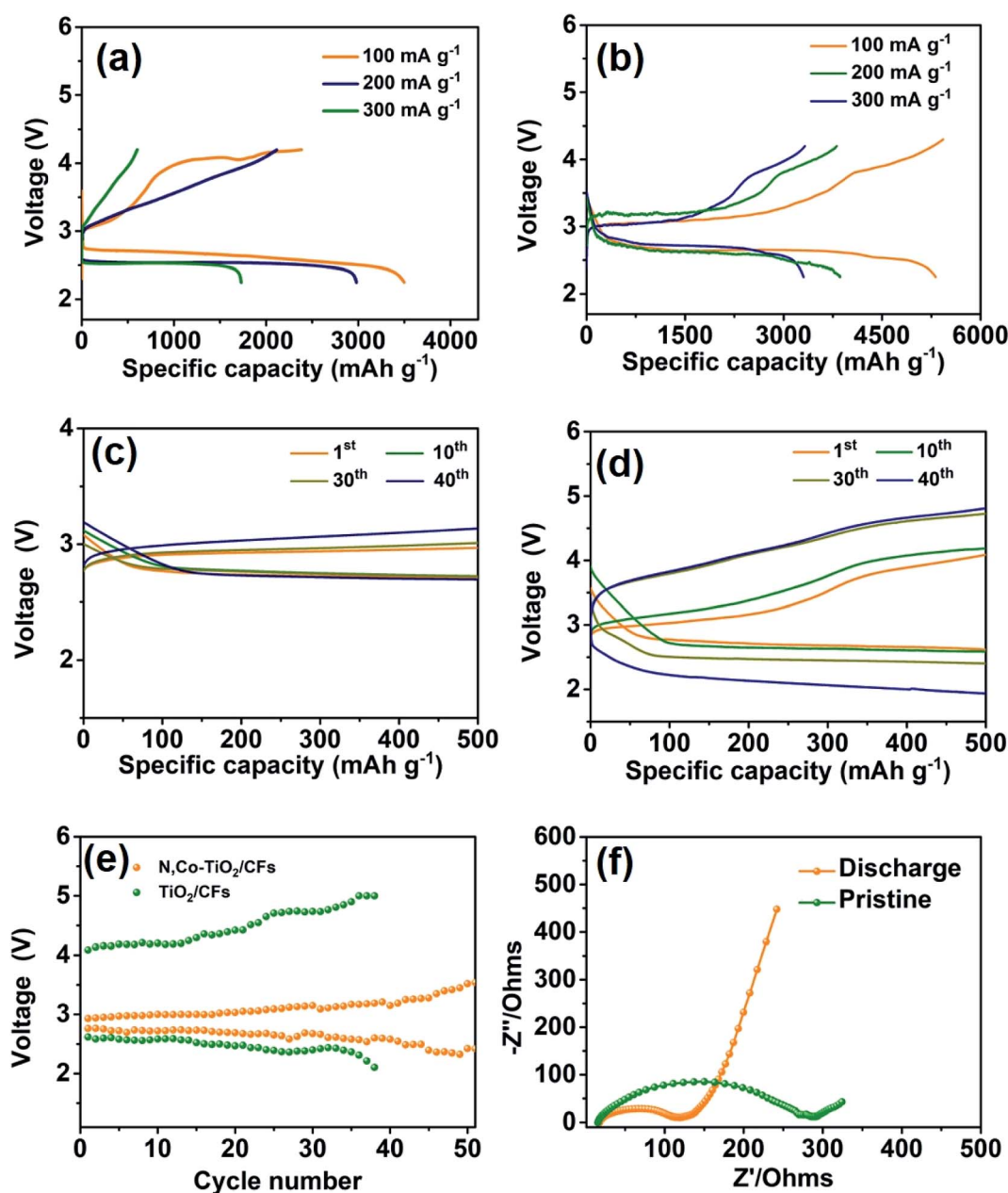Density functional theory (DFT) calculations were carried out to study the binding energies between LiO$_2$ and different

Fig. 5 The rate performance of (a) TiO$_2$/CFs and (b) N,Co-TiO$_2$/CFs. The discharge/charge profiles of (c) N,Co-TiO$_2$/CFs and (d) TiO$_2$/CFs at a current density of 200 mA g^{-1} with a limited capacity of 500 mA h g^{-1}. (e) The charge and discharge terminal potential of N,Co-TiO$_2$/CFs and TiO$_2$/CFs with a fixed specific capacity of 500 mA h g^{-1}. (f) Electrochemical impedance spectra of pristine and discharged N,Co-TiO$_2$/CFs.

23052 | J. Mater. Chem. A, 2019, 7, 23046–23054

This journal is © The Royal Society of Chemistry 2019

catalysts, including TiO_2/CFs, $N-TiO_2/CFs$, $Co-TiO_2/CFs$ and $N,Co-TiO_2/CFs$ (Fig. 4). The (110) plane of rutile TiO_2 was used to evaluate the adsorption energies. The (110) plane of TiO_2 in different catalysts was optimized and relaxed before calculating the adsorption energies. The reconstruction of the atoms, particularly the Co atom, can be observed on the plane of $N,Co-TiO_2/CFs$. In the $N,Co-TiO_2/CF$ electrode, Li atoms preferably adsorbed onto the Co atom in the discharge process. After the addition of oxygen molecules, strong affinity of LiO_2 to the (110) surface of TiO_2 with a binding energy of -4.08 eV is achieved. The binding energy is comparable to that of Li_2O_2 to a variety of catalysts,[47,48] suggesting that LiO_2 is also stable. When LiO_2 was adsorbed onto the surface of TiO_2/CFs, $N-TiO_2/CFs$ and $Co-TiO_2/CFs$, the binding energy with the adsorption sites of O, N, and Co is -2.30, -3.45, and -1.41 eV (ESI, Table S1†), respectively. The decrease in the adsorption energy between LiO_2 and $N,Co-TiO_2/CFs$ suggests that the disproportionation of LiO_2 could be suppressed.[29,31] As a result, the $N,Co-TiO_2/CF$ cathode prevents the disproportionation of LiO_2 and thus enhances the electrochemical performance.

With the stabilization of the discharge product LiO_2, $N,Co-TiO_2/CFs$ also displays superior rate performance (Fig. 5a and b). Specific discharge capacities of 5400, 3800, and 3200 mA h g^{-1} are achieved at current densities of 100, 200, and 300 mA g^{-1}, respectively. However, the specific discharge capacity of TiO_2/CFs is less than 1750 mA h g^{-1} at a current density of 300 mA g^{-1}. The remarkably high rate capability can be ascribed to the formation of conductive LiO_2 with the high catalytic activity $N,Co-TiO_2/CFs$. Moreover, the overpotential of $N,Co-TiO_2/CFs$ during the charge process is also far lower than that of TiO_2/CFs at the same current density. The reduced overpotential of $N,Co-TiO_2/CFs$ can be attributed to the fast decomposition of LiO_2.

The cycling performance of $N,Co-TiO_2/CFs$ and TiO_2/CFs was evaluated at 200 mA g^{-1} with a cutoff capacity of 500 mA h g^{-1} and 1000 mA h g^{-1} (Fig. 5c and the ESI, Fig. S13†). The initial discharge terminal voltage of $N,Co-TiO_2/CFs$ is approximately 2.75 V (Fig. 5c), close to 2.76 V, the theoretical formation potential of LiO_2. The subsequent charge terminal potential is only 3.0 V, giving an overpotential of 0.25 V, much lower than that of TiO_2/CFs (Fig. 5d). The charge terminal potential of $N,Co-TiO_2/CFs$ is still less than 3.5 V for 50 cycles (Fig. 5e). In contrast, a dramatic increase in the charge terminal potential upon cycling is observed for TiO_2/CFs (Fig. 5e). The superior performance of $N,Co-TiO_2/CFs$ might be attributed to the formation LiO_2 with high electronic and ionic conductivity.

Electrochemical impedance spectroscopy (EIS) of $N,Co-TiO_2/CFs$ and TiO_2/CFs was performed from 0.01 Hz to 100 kHz (Fig. 5f and the ESI, Fig. S14†). The semicircle in the high frequency region is ascribed to the charge-transfer resistance (R_{ct}), including the interfacial resistance of the electrolyte and the catalyst. $N,Co-TiO_2/CFs$ shows an obvious decrease in the ohmic resistance after discharge, indicating the improvement in conductivity induced by the formation of LiO_2 on $N,Co-TiO_2/CFs$. The line in the low frequency region corresponding to the Warburg impedance is associated with Li^+ ion transfer from the electrode surface to the electrode/electrolyte interface. A slope close to 45 degree is obtained for $N,Co-TiO_2/CFs$, indicating fast Li^+ diffusion to the electrode. After discharge, significant charge-transfer resistance was observed for TiO_2/CFs (Fig. S14†). The increased resistance might be a result of the low electronic conductivity of Li_2O_2 formed on the surface of discharged TiO_2/CFs.

4. Conclusions

Excellent electrical performance of $Li-O_2$ batteries was achieved by the formation of LiO_2 with a non-noble metal catalyst, $N,Co-TiO_2/CFs$. The $Li-O_2$ batteries based on LiO_2 present a very low charge potential (about 0.2 V), long cycle stability and high rate capability. N,Co-codoped TiO_2 plays a vital role in the generation of LiO_2 during the discharge and charge process. Raman spectroscopy, galvanostatic intermittent titration, and differential quantitative mass spectrometry indicate the existence of LiO_2 in the discharge process. The density functional theory calculation results show the stability mechanism of LiO_2. This work provides a new approach to settle the critical problems in current $Li-O_2$ batteries with the involvement of non-noble metals.

Contribution

K. Wang and J. Chen proposed and supervised the project. W. Bai designed the experiments and wrote the manuscript. S. Xu, C. Xu, Q. Zhang, H. Wang, Z. Zhang, X. Chen, S. Dong, Y. Liu, Z. Wang and Z. Xu participated in analyzing the experimental results and X. Zhang participated in discussion. All authors have approved the final version of the manuscript.

Conflicts of interest

There are no conflicts to declare.

Acknowledgements

References

1 B. Kim, J. Shin, Y. Mun, J. Lee and J. Choi, *ACS Nano*, 2017, **11**, 1736–1746.

2 Z. Chang, J. Xu and X. Zhang, *Adv. Energy Mater.*, 2017, **7**, 1700875.

3 W. B. Luo, T. V. Pham, H. P. Guo, H. K. Liu and S. X. Dou, *ACS Nano*, 2017, **11**, 1747–1754.

4 H. Wu, W. Sun, Y. Wang, F. Wang, J. Liu, X. Yue, Z. Wang and K. Sun, *ACS Appl. Mater. Interfaces*, 2017, **9**, 12355–12365.

5 J. J. Xu, Z. L. Wang and X. B. Zhang, *Nat. Commun.*, 2013, **4**, 2438.

6 S. Matsuda, K. Uosaki and S. Nakanishi, *J. Power Sources*, 2017, **353**, 138–143.

7 M. Nazarian-Samani, H.-D. Lim and K.-B. Kim, *J. Mater. Chem. A*, 2017, **5**, 619–631.

8 A. Arul, M. Christy and K. S. Nahm, *Electrochim. Acta*, 2016, **218**, 335–344.

9 A. Arul, H. Pak, K. U. Moon and K. S. Nahm, *Appl. Catal., B*, 2018, **220**, 488–496.

10 B. J. Bergner, A. Schurmann, K. Peppler and J. Janek, *J. Am. Chem. Soc.*, 2014, **136**, 15054–15064.

11 Y. Chen, X. Gao and P. G. Bruce, *Nat. Commun.*, 2018, **9**, 767.

12 N. Feng, X. Mu, X. Zhang, P. He and H. Zhou, *ACS Appl. Mater. Interfaces*, 2017, **9**, 3733–3739.

13 X. Hu, J. Wang, Z. Li, J. Wang, D. H. Gregory and J. Chen, *Nano Lett.*, 2017, **17**, 2073–2078.

14 D. Kundu, R. Black, B. Adams and L. F. Nazar, *ACS Cent. Sci.*, 2015, **1**, 510–515.

15 W.-J. Kwak, S.-J. Park, H.-G. Jung and Y.-K. Sun, *Adv. Energy Mater.*, 2018, **8**, 1702258.

16 Y. Li, S. Dong, B. Chen, C. Lu, K. Liu, Z. Zhang, H. Du, X. Wang, X. Chen, X. Zhou and G. Cui, *J. Phys. Chem. Lett.*, 2017, **8**, 4218–4225.

17 Z. Liang and Y. C. Lu, *J. Am. Chem. Soc.*, 2016, **138**, 7574–7583.

18 S. Matsuda, S. Mori, K. Hashimoto and S. Nakanishi, *J. Phys. Chem. C*, 2014, **118**, 28435–28439.

19 D. Sharon, P. Sharon, D. Hirshberg, M. Salama, M. Afri, L. J. W. Shimon, W. J. Kwak, Y. K. Sun, A. A. Frimer and D. Aurbach, *J. Am. Chem. Soc.*, 2017, **139**, 11690–11693.

20 D. Sun, Y. Shen, W. Zhang, L. Yu, Z. Yi, W. Yin, D. Wang, Y. Huang, J. Wang, D. Wang and J. B. Goodenough, *J. Am. Chem. Soc.*, 2014, **136**, 8941–8946.

21 W. Fan, B. Wang, X. Guo, X. Kong and J. Liu, *Nano Energy*, 2016, **27**, 577–586.

22 D. J. Lee, H. Lee, Y. J. Kim, J. K. Park and H. T. Kim, *Adv. Mater.*, 2016, **28**, 857–863.

23 B. Liu, W. Xu, J. Tao, P. Yan, J. Zheng, M. H. Engelhard, D. Lu, C. Wang and J.-G. Zhang, *Adv. Energy Mater.*, 2018, **8**, 1702340.

24 N. Togasaki, R. Shibamura, T. Naruse, T. Momma and T. Osaka, *APL Mater.*, 2018, **6**, 047704.

25 J. J. Xu, Q. C. Liu, Y. Yu, J. Wang, J. M. Yan and X. B. Zhang, *Adv. Mater.*, 2017, **29**, 1606552.

26 J. Zhu, J. Yang, J. Zhou, T. Zhang, L. Li, J. Wang and Y. Nuli, *J. Power Sources*, 2017, **366**, 265–269.

27 R. Black, S. H. Oh, J. H. Lee, T. Yim, B. Adams and L. F. Nazar, *J. Am. Chem. Soc.*, 2012, **134**, 2902–2905.

28 U. Das, K. C Lau, P. C. Redfern and L. A. Curtiss, *J. Phys. Chem. Lett.*, 2014, **5**, 813–819.

29 R. Gao, X. Liang, P. Yin, J. Wang, Y. L. Lee, Z. Hu and X. Liu, *Nano Energy*, 2017, **41**, 535–542.

30 P. Hartmann, C. L. Bender, M. Vracar, A. K. Durr, A. Garsuch, J. Janek and P. Adelhelm, *Nat. Mater.*, 2013, **12**, 228.

31 J. Lu, L. Y. Jung, X. Luo, L. K. Chun, M. Asadi, H.-H. Wang, S. Brombosz, J. Wen, D. Zhai, Z. Chen, D. J. Miller, Y. Jeong, J. Park, Z. Fang, B. Kumar, A. Khojin, Y. Sun, L. Curtiss and K. Amine, *Nature*, 2016, **529**, 377.

32 X. Ren and Y. Wu, *J. Am. Chem. Soc.*, 2013, **135**, 2923–2926.

33 Z. Sadighi, J. Huang, L. Qin, S. Yao, J. Cui and J. K. Kim, *J. Power Sources*, 2017, **365**, 134–147.

34 J. Yang, D. Ma, Y. Li, P. Zhang, H. Mi, L. Deng, L. Sun and X. Ren, *J. Power Sources*, 2017, **360**, 215–220.

35 J. Yang, D. Zhai, H. H. Wang, K. C. Lau, J. A. Schlueter, P. Du, D. J. Myers, Y. K. Sun, L. Curtiss and K. Amine, *Phys. Chem. Chem. Phys.*, 2013, **15**, 3764–3771.

36 X. Zhang, L. Guo, L. Gan, Y. Zhang, J. Wang, L. Johnson, P. Bruce and Z. Peng, *J. Phys. Chem. C*, 2017, **8**, 2334–2338.

37 Q. Liu, J. Xu, D. Xu and X. Zhang, *Nat. Commun.*, 2015, **6**, 7892.

38 J. Kang, J. Kim, S. Lee, S. Wi, C. Kim, S. Hyun, S. Nam, Y. Park and B. Park, *Adv. Energy Mater.*, 2017, **7**, 1700814.

39 Y. Zhang, C. Li, C. Pan and J. McKittrick, *J. Am. Chem. Soc.*, 2012, **95**, 2951–2956.

40 X. Dan, K. L. Yao, G. Y. Gao and L. Yang, *J. Magn. Magn. Mater.*, 2013, **335**, 18–124.

41 S. Hyun and S. Shanmugam, *J. Power Sources*, 2017, **354**, 48–56.

42 S. Liu, Q. Li, C. Hou, X. Feng and Z. Guan, *J. Alloys Compd.*, 2013, **575**, 128–136.

43 G. Tan, L. Chong, R. Amine, J. Lu, C. Liu, Y. Yuan, J. Wen, K. He, X. Bi, Y. Guo, H. Wang, R. Shahbazian-Yassar, S. Hallaj, D. Miller, D. Liu and K. Amine, *Nano Lett.*, 2017, **17**, 2959–2966.

44 J. Wang, Y. F. Zhao, T. Wang, H. Li and C. Li, *Phys. B*, 2015, **478**, 6–11.

45 S. Zhang, Z. Huang, Z. Wen, L. Zhang, J. Jin, R. Yassar and J. Yang, *Nano Lett.*, 2017, **17**, 3518–3526.

46 W. Kwak, J. Park, H. Jung and W. Kwak, *ACS Energy Lett.*, 2017, **2**, 2756–2760.

47 Z. Sadighi, J. Liu and F. Ciucci, *Nanoscale*, 2018, **10**, 15588–15599.

48 Z. Sadighi, J. Liu, F. Ciucci and J. Kim, *Nanoscale*, 2018, **10**, 22549–22559.